



A new analytic approach to infer the cosmic-ray ionization rate in hot molecular cores from HCO^+ , N_2H^+ ,

Downloaded from: <https://research.chalmers.se>, 2024-11-19 16:37 UTC

Citation for the original published paper (version of record):

Luo, G., Bisbas, T., Padovani, M. et al (2024). A new analytic approach to infer the cosmic-ray ionization rate in hot molecular cores from HCO^+ , N_2H^+ , and CO observations. *Astronomy and Astrophysics*, 690. <http://dx.doi.org/10.1051/0004-6361/202450285>

N.B. When citing this work, cite the original published paper.

A new analytic approach to infer the cosmic-ray ionization rate in hot molecular cores from HCO⁺, N₂H⁺, and CO observations

Gan Luo^{1,*}, Thomas G. Bisbas², Marco Padovani³, and Brandt A. L. Gaches⁴

¹ Institut de Radioastronomie Millimetrique, 300 rue de la Piscine, 38400 Saint-Martin d'Hères, France

² Research Center for Astronomical Computing, Zhejiang Laboratory, Hangzhou 311100, China

³ INAF-Osservatorio Astrofisico di Arcetri, Largo E. Fermi 5, 50125 Firenze, Italy

⁴ Department of Space, Earth and Environment, Chalmers University of Technology, Gothenburg 412 96, Sweden

Received 8 April 2024 / Accepted 11 September 2024

ABSTRACT

Context. The cosmic-ray ionization rate (ζ_2) is one of the key parameters in star formation, since it regulates the chemical and dynamical evolution of molecular clouds by ionizing molecules and determining the coupling between the magnetic field and gas.

Aims. However, measurements of ζ_2 in dense clouds (e.g., $n_{\text{H}} \geq 10^4 \text{ cm}^{-3}$) are difficult and sensitive to the model assumptions. The aim is to find a convenient analytic approach that can be used in high-mass star-forming regions (HMSFRs), especially for warm gas environments such as hot molecular cores (HMCs).

Methods. We propose a new analytic approach to calculate ζ_2 through HCO⁺, N₂H⁺, and CO measurements. By comparing our method with various astrochemical models and with observations found in the literature, we identify the parameter space for which the analytic approach is applicable.

Results. Our method gives a good approximation, to within 50%, of ζ_2 in dense and warm gas (e.g., $n_{\text{H}} \geq 10^4 \text{ cm}^{-3}$, $T = 50, 100 \text{ K}$) for $A_{\text{V}} \geq 4 \text{ mag}$ and $t \geq 2 \times 10^4 \text{ yr}$ at Solar metallicity. The analytic approach gives better results for higher densities. However, it starts to underestimate ζ_2 at low metallicity ($Z = 0.1 Z_{\odot}$) when the value is too high ($\zeta_2 \geq 3 \times 10^{-15} \text{ s}^{-1}$). By applying our method to the OMC-2 FIR4 envelope and the L1157-B1 shock region, we find ζ_2 values of $(1.0 \pm 0.3) \times 10^{-14} \text{ s}^{-1}$ and $(2.2 \pm 0.4) \times 10^{-16} \text{ s}^{-1}$, consistent with those previously reported.

Conclusions. We calculate ζ_2 toward a total of 82 samples in HMSFRs, finding that the average value of ζ_2 toward all HMC samples ($\zeta_2 = (7.4 \pm 5.0) \times 10^{-16} \text{ s}^{-1}$) is more than an order of magnitude higher than the theoretical prediction of cosmic-ray attenuation models, favoring the scenario that locally accelerated cosmic rays in embedded protostars should be responsible for the observed high ζ_2 .

Key words. astrochemistry – stars: formation – ISM: abundances – ISM: clouds – cosmic rays – ISM: molecules

1. Introduction

Cosmic rays (CRs) play a major role in the physical and chemical evolution of dense clouds. In well-shielded regions where far-ultraviolet (FUV) photons cannot penetrate, namely where the visual extinction (A_{V}) is larger than 3–4 mag (Wolfire et al. 2010), CRs initiate the chemistry by ionizing various molecules and producing ions (e.g., H₃⁺)¹. On the other hand, CRs determine the degree of ionization in dense clouds and regulate the coupling between the magnetic field and gas, which, in turn, affects the dynamic timescale during the star formation process (Dalgarno 2006; Padovani et al. 2014, 2020; Padovani & Gaches 2024).

Ions (e.g., H₃⁺ and H_nO⁺) are the most favored tracers to constrain the cosmic-ray ionization rate (CRIR), since the formation and destruction of these species are relatively simple and allow us to estimate almost directly the CRIR (Gerin et al. 2010; Indriolo & McCall 2012; Indriolo et al. 2015; Neufeld & Wolfire 2017). In dense clouds, such methodology is, however, not available due to the large extinction and low abundance of the above-mentioned ions.

The abundance ratios of DCO⁺/HCO⁺ and HCO⁺/CO had been proposed to infer the ionization fraction and CRIR in cold prestellar cores (Caselli et al. 1998). However, the deuteration ratios are sensitive to the initial ortho-to-para ratio, the evolution timescale, and the source physical conditions (e.g., gas density and temperature, Shingledecker et al. 2016). Thus, the resultant CRIR from the above method could be overestimated by several orders of magnitude (Sabatini et al. 2023; Redaelli et al. 2024). More recently, an analytic approach using ortho-H₂D⁺ and CO was proposed to estimate the CRIR (Bovino et al. 2020) in cold prestellar cores where depletion of molecules is crucial. In addition, rovibrational H₂ lines could be a potentially useful method to derive CRIR value in the cold molecular cloud (Bialy 2020; Padovani et al. 2022; Bialy et al. 2022; Gaches et al. 2022a), which would be, in principle, detected by the *James Webb* Space Telescope (JWST).

In high-mass star-forming regions (HMSFRs), the gas temperature increases in the more evolved phase (e.g., $T \sim 100 \text{ K}$ in hot molecular cores, HMCs, Blake et al. 1987; Beuther et al. 2007b; Luo et al. 2019; Qin et al. 2022), depletion and deuteration are inefficient, so that the methods described above cannot be adopted. Over the past decade, different molecular line tracers combined with astrochemical models have been used to probe the CRIR in HMSFRs, such as HCO⁺ and N₂H⁺ (Ceccarelli et al. 2014b; Redaelli et al. 2021), and carbon-chain molecules (e.g., HC₃N, HC₅N, Fontani et al. 2017; Favre et al. 2018). While chemical modeling requires large computational resources, a

* Corresponding author; luo@iram.fr;
tbisbas@zhejianglab.com

¹ Assuming no other sources of ionization (e.g., X-rays in the vicinity of supernova remnants, Yusef-Zadeh et al. 2003; Indriolo 2023).

convenient analytic approach would be useful in determining the variance of CRIR with the spatial distribution and evolution stage in HMSFRs.

In this work, we propose a new analytic approach to estimate the CRIR in HMSFRs, especially for high-mass protostellar objects (HMPOs) and HMCs. HMPOs are in a more evolved phase than the cold infrared dark cloud (IRDC). They consist of massive accreting protostars (e.g., $M > 8 M_{\odot}$) and exhibit bright mid-infrared emission and strong outflows (Beuther et al. 2002b, 2007a; Zinnecker & Yorke 2007; Motte et al. 2018). The characteristic size of HMPOs is ~ 0.5 pc and the average density is between 10^4 and 10^6 cm^{-3} (Beuther et al. 2002a). HMCs appear in the later stage of HMPOs and are characterized by high gas temperatures (e.g., $T \gtrsim 100$ K), densities ($n_{\text{H}} \gtrsim 10^6 \text{ cm}^{-3}$), and rich molecular lines (Blake et al. 1987; Kurtz et al. 2000; Beuther et al. 2007b; Qin et al. 2022). We compare our approach with chemical simulations from 3D-PDR and UCLCHEM and demonstrate that our method can give a good estimation of CRIR for HMPOs and HMCs.

The paper is organized as follows. We present the chemical analysis and describe the analytic approach in Sect. 2. In Sect. 3, we compare our approach with chemical simulations. We apply our method to two well-known sources and compare our results with previous modeling in the literature in Sect. 4. The uncertainties and robustness of the approach are also discussed. In Sect. 5, we calculate the CRIR toward a large sample of HMSFRs. The main results and conclusions are summarized in Sect. 6.

2. Methods

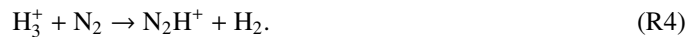
2.1. Chemical analysis

We describe, below, the formation and destruction reactions of H_3^+ , HCO^+ , N_2H^+ , and H_3O^+ in dense and warm clouds (e.g., $n_{\text{H}} \geq 10^4 \text{ cm}^{-3}$, $T \geq 50$ K), where the depletion is negligible.

The formation of H_3^+ in dense clouds starts from the ionization of H_2 by CRs (see, e.g., Glassgold & Langer 1973):



Then, H_3^+ can be removed by the most abundant neutral species (Indriolo & McCall 2012):



and electrons:



Reactions (R3) and (R4) are the main formation channels of HCO^+ and N_2H^+ , respectively.

The corresponding destruction channels of HCO^+ and N_2H^+ are (Dalgarno 2006):



² Reaction (R8) below also contribute to the formation of HCO^+ but with a minor role.

and



Considering reactions (R1)–(R6), CRIR (ζ_2 , referring to the ionization rate of H_2) can be written as:

$$\zeta_2 = \frac{n(\text{H}_3^+)}{n(\text{H}_2)} [n(\text{CO})k_{\text{R3}} + n(\text{N}_2)k_{\text{R4}} + n(\text{O})k_{\text{R5}} + n(\text{e}^-)k_{\text{R6}}]. \quad (1)$$

Similarly, from reactions (R4) and (R8)–(R10) we can write:

$$n(\text{H}_3^+)n(\text{N}_2)k_{\text{R4}} = n(\text{N}_2\text{H}^+) [n(\text{CO})k_{\text{R8}} + n(\text{e}^-)k_{\text{R9}} + n(\text{O})k_{\text{R10}}]. \quad (2)$$

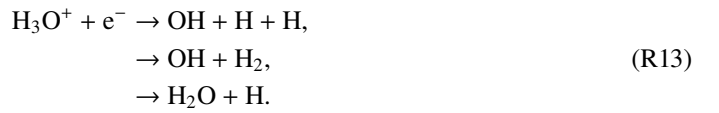
Considering the charge balance, the number density of electrons should be equal to the most abundant ions (see Appendix A):

$$n(\text{e}^-) = n(\text{HCO}^+) + n(\text{N}_2\text{H}^+) + n(\text{H}_3^+) + n(\text{H}_3\text{O}^+). \quad (3)$$

In dense clouds, the formation of H_3O^+ starts from reaction (R5). Then, it hydrogenates to form H_2O^+ and H_3O^+ (Bialy & Sternberg 2015; Indriolo et al. 2015; Luo et al. 2023b):



Electron recombination reactions dominate the destruction of H_3O^+ :



From reactions (R5), (R10), and (R11)–(R13), $n(\text{H}_3\text{O}^+)$ can be written as:

$$n(\text{H}_3\text{O}^+) = \frac{n(\text{O})n(\text{H}_3^+)k_{\text{R5}} + n(\text{N}_2\text{H}^+)n(\text{O})k_{\text{R10}}}{n(\text{e}^-)k_{\text{R13}}}. \quad (4)$$

Combining Eqs. (3) and (4), $n(\text{H}_3^+)$ can be written as:

$$n(\text{H}_3^+) = \frac{n(\text{e}^-)^2 - n(\text{e}^-) [n(\text{HCO}^+) + n(\text{N}_2\text{H}^+)] - \alpha}{n(\text{e}^-) + n(\text{O})k_{\text{R5}}/k_{\text{R13}}}, \quad (5)$$

where α is

$$\alpha = \frac{n(\text{N}_2\text{H}^+)n(\text{O})k_{\text{R10}}}{k_{\text{R13}}}, \quad (6)$$

Then, $n(\text{e}^-)$ can be calculated from Eqs. (2) and (5):

$$n(\text{e}^-) = \frac{\beta + \sqrt{\beta^2 + 4\gamma\theta}}{2\gamma}, \quad (7)$$

where

$$\begin{aligned} \beta &= \frac{n(\text{N}_2\text{H}^+)}{n(\text{N}_2)k_{\text{R4}}} \left[\frac{n(\text{O})k_{\text{R5}}k_{\text{R9}}}{k_{\text{R13}}} + n(\text{CO})k_{\text{R8}} + n(\text{O})k_{\text{R10}} \right] \\ &\quad + n(\text{HCO}^+) + n(\text{N}_2\text{H}^+), \end{aligned} \quad (8)$$

$$\gamma = 1 - \frac{n(\text{N}_2\text{H}^+)\text{k}_{\text{R}9}}{n(\text{N}_2)\text{k}_{\text{R}4}}, \quad (9)$$

and

$$\theta = \alpha \left[1 + \text{k}_{\text{R}5} \frac{n(\text{CO})\text{k}_{\text{R}8} + n(\text{O})\text{k}_{\text{R}10}}{n(\text{N}_2)\text{k}_{\text{R}4}\text{k}_{\text{R}10}} \right]. \quad (10)$$

To determine ζ_2 through our new methodology it is needed:

1. a proper constraint on $n(\text{H}_2)$;
2. to determine the abundances of HCO^+ , N_2H^+ , and CO from observations;
3. an assumption of the initial abundances of N_2 and O.

In dense cores where hydrogen is mostly in molecular form, we can divide all number density terms ($n(x)$) by $n(\text{H}_2)$ in Eqs. (1)–(7). Thus, the calculated CRIR ($\tilde{\zeta}_2$, we distinguish between the calculated CRIR ($\tilde{\zeta}_2$) and the input one (ζ_2) from chemical simulations) can be written as:

$$\tilde{\zeta}_2 = n(\text{H}_2)f(\text{H}_3^+) [f(\text{CO})\text{k}_{\text{R}3} + f(\text{N}_2)\text{k}_{\text{R}4} + f(\text{O})\text{k}_{\text{R}5} + f(\text{e}^-)\text{k}_{\text{R}6}], \quad (11)$$

where $f(x)$ is the relative abundance of species “x” with respect to H_2 , $n(\text{H}_2)$ is the number density of H_2 , and $f(\text{e}^-)$ can be obtained from Eq. (7). For the calculations of $\tilde{\zeta}_2$, we use the latest reaction rates from the UMIST database (hereafter, UMIST2022, Millar et al. 2024) unless otherwise stated.

2.2. Chemical models

To explore the behavior of our analytic approach, we employ the publicly available astrochemical codes³ 3D-PDR (Bisbas et al. 2012) and UCLCHEM (Holdship et al. 2017). 3D-PDR is a photodissociation region code that models one- and three-dimensional density distributions. It calculates the attenuation of the FUV radiation field in every depth point and outputs the self-consistent solutions of chemical abundances, gas and dust temperature, emissivities, and level populations by performing iterations over thermal balance. In the 3D-PDR models, we consider more than 200 species with 3000 reactions taken from the UMIST2012⁴ (McElroy et al. 2013). The initial gas phase abundances of different elements are listed in Table 1. We note that the initial element abundances are not expected to be the same everywhere. However, as long as the abundances of key species do not change significantly, the assumptions and conclusions in Sect. 2 remain valid (see Sect. 4.1.1 for more discussion on different metallicities). We also consider the treatment of CR attenuation incorporated into 3D-PDR, as presented in Gaches et al. (2019, 2022b). Unless otherwise stated, all 3D-PDR models presented here are calculated until the thermal balance is reached.

We perform additional simulations with UCLCHEM (Holdship et al. 2017) to test how the gas-grain reactions and depletion processes influence the results. UCLCHEM is a time-dependent astrochemical code focusing on gas-grain reactions. It considers freeze-out processes, thermal, and non-thermal desorption processes and outputs the chemical abundances at a given temperature, density, and A_V . Contrary to 3D-PDR

Table 1. Initial gas-phase element abundances used in our simulations.

Elements	Abundance relative to H	References
H	5×10^{-1}	/
H_2	2.5×10^{-1}	/
He	9×10^{-2}	a
C^+	1.5×10^{-4}	b,c
O	3×10^{-4}	d,e
N	7.6×10^{-5}	f
S^+	8×10^{-8}	c, g
Si^+	8×10^{-9}	c, g
Mg^+	7×10^{-9}	c, g
Fe^+	3×10^{-9}	c, g
Na^+	2×10^{-9}	c, g
P^+	2×10^{-10}	c, g
Cl^+	1×10^{-9}	c, g
F^+	6.68×10^{-9}	h

Notes. References: (a) Wakelam & Herbst (2008). (b) Sofia et al. (1997). (c) Hincelin et al. (2011). (d) Meyer et al. (1998). (e) Lis et al. (2023). (f) Meyer et al. (1997). (g) Majumdar et al. (2017). (h) Neufeld et al. (2005).

calculations where the code terminates as long as the thermal balance is reached, the simulations in UCLCHEM are isothermal. We set three temperatures in these simulations, $T_k = 15, 50$, and 100 K. The typical temperature of the cold dark cloud is 15 K and it is below the temperature for CO desorption ($T \sim 20$ K) (Öberg et al. 2011). The second chosen temperature (50 K) is above the sublimation temperature of simple molecules (e.g., CO) but below the desorption temperature of water ice and COMs. The third chosen temperature (100 K) is the typical temperature of HMCs and most of the species would be released from the ice phase (van Dishoeck 2014).

In UCLCHEM simulations, the deuterium chemical network of Majumdar et al. (2017) is adopted. To reduce the computational expense, species with molecular weight higher than 66 were excluded (mostly carbon-chain molecules and complex organic molecules that contain more than 5 carbon atoms). Excluding these molecules may not greatly impact the results since they gradually build up the abundances from C and C^+ , and have little chemical connection with the simple species we mentioned above. Besides, their abundances are usually too low (e.g., 10^{-10} and below, Herbst & van Dishoeck 2009) to impact the simple species. The chemical network contains a total of ~ 800 species and $\sim 3 \times 10^4$ reactions. The initial gas-phase abundance of HD is adopted as the value measured in the Local Bubble (1.6×10^{-5} , Linsky et al. 2006)⁵. The remaining element abundances are the same as in Table 1. For all the simulations in both 3D-PDR and UCLCHEM, the cloud radius is set as 1 pc.

3. Results

3.1. Comparison to 3D-PDR simulations

We test three uniform density clouds ($n_{\text{H}} = 10^4, 10^5$, and 10^6 cm^{-3}) with different uniform CRIR ($10^{-19} \leq \zeta_2/\text{s}^{-1} \leq 10^{-14}$)

³ <https://uclchem.github.io/>

⁴ We note that the reaction rates of (R5), (R8), (R11), and (R12) have changed by up to a factor of ~ 3 between the UMIST2012 and UMIST2022. In that case, we calculate $\tilde{\zeta}_2$ in Sect. 3.1 using the reaction rates from UMIST2012 only when comparing with 3D-PDR simulations.

⁵ The measured D/H ratios in high column density regions are lower, presumably due to the depletion of D on dust grain (Linsky et al. 2006; Friedman et al. 2023). However, the D/H ratio only matters in our analysis for the dark cloud where depletion of molecules is significant (see Sect. 3.2).

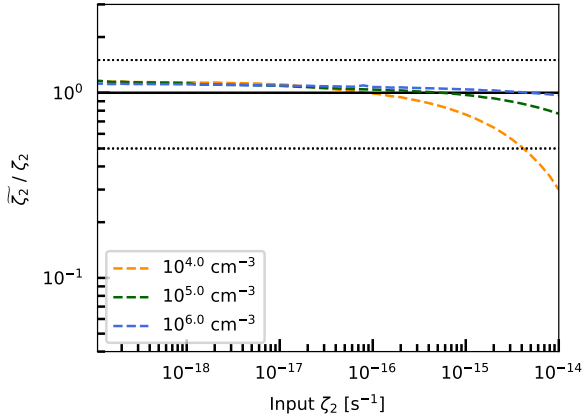


Fig. 1. Comparison between our approach and 3D-PDR simulations. The x-axis denotes the input CRIR of each simulation, where the CRIR in each simulation is treated as uniform. The y-axis denotes the ratio between the calculated CRIR and the input one ($\tilde{\zeta}_2/\zeta_2$) at $A_V = 20$ mag. The black horizontal line represents the fiducial value and the horizontal dotted lines represent 50% of the deviation from the input values. Orange, green, and blue dashed lines represent results at $n_H = 10^4$, 10^5 , and 10^6 cm^{-3} . The external FUV intensity for all simulations is normalized to the Draine unit ($\chi/\chi_0 = 1$).

input. Figure 1 shows the ratio between CRIR derived from Eq. (11) and the input value ($\tilde{\zeta}_2/\zeta_2$) at $A_V = 20$ mag. In most of the simulations, the calculated CRIR from the analytic approach is within 50% of the model input. The analytic approach underestimates the input CRIR by up to a factor of 3 at $n_H = 10^4$ cm^{-3} and $\zeta_2 = 10^{-14}$ s^{-1} . This is due to the destruction of CO molecules under high CRIR (Bialy & Sternberg 2015; Bisbas et al. 2015, 2017), thus, the destruction pathways we analyzed in Sect. 2 change. As the density increases, the analytic approach gives a more accurate result.

Figure 2 shows the deviation maps between the analytic approach and the input values at different A_V and ζ_2 . Our analytic approach gives a good approximation, to within 50%, if $\zeta_2 \leq 5 \times 10^{-15}$ s^{-1} and $A_V \geq 4$ mag at $n_H = 10^4$ cm^{-3} , and $A_V \geq 4$ mag for any ζ_2 at $n_H = 10^5$ cm^{-3} and $n_H = 10^6$ cm^{-3} .

In addition, we test the CR attenuation model with a variable density distribution, in which the CR spectrum is adopted as the high-energy spectrum model \mathcal{H} from Ivlev et al. (2015) and the density distribution of the cloud adopts the A_V - n_H relation of Bisbas et al. (2023). This relation has been found to reproduce reasonably well and at a minimal computational cost, the results from computationally expensive three-dimensional astrochemical models. Figure 3 shows the comparison between the input ζ_2 and the analytical approach. At lower column densities ($N_{H_2} < 3.4 \times 10^{21}$ cm^{-2} , corresponding to $n_H < 3 \times 10^3$ cm^{-3}), our approach underestimates ζ_2 by over 50%. At higher column densities, our approach gives a good approximation.

3.2. Comparison to UCLCHEM simulations

Figure 4 shows the comparison between the analytic approach with UCLCHEM simulations for different temperatures and densities. At low temperatures ($T_k = 15$ K), most of the species (including CO and O) would freeze out onto dust grain, the analytic approach underestimates the CRIR by a factor from a few ($n_H = 10^4$ cm^{-3}) to several orders of magnitude (at $n_H = 10^5$ and 10^6 cm^{-3}). This is expected since the depletion processes greatly reduce the abundances of CO, O, and N_2 by several orders of magnitude such that the destruction pathways of H_3^+

we considered in Sect. 2 (reactions (R3)-(R5)) are no longer the dominant H_3^+ destruction mechanism. Instead, deuteration fractionation cannot be ignored such that the destruction of H_3^+ and the reaction channels should involve deuterated species (Millar et al. 1989; Ceccarelli et al. 2014a; Caselli et al. 2019).

When the gas temperature is higher than the sublimation temperature of CO (the cases of $T_k = 50$ and 100 K), the analytic approach gives a better estimation, to within 50% for most cases. The higher the gas temperature, the better estimation is given by the analytic approach. Our analytic approach gives a more accurate estimation for higher density simulations, the same as we found with the 3D-PDR simulations.

Figure 5 shows the deviation map between the analytic approach and the input values at different evolution timescales and ζ_2 . For early timescales, where the molecules are still building their abundances (e.g., at $n_H = 10^4$ cm^{-3} and $t \leq 10^4$ yr), the analytic approach underestimates the CRIR. At $n_H = 10^4$ cm^{-3} and $t \geq 2 \times 10^4$ yr, the analytic approach gives a reasonable ζ_2 estimation except for $t \approx 10^5$ yr and $\zeta_2 \approx 5 \times 10^{-16}$ s^{-1} , where the calculated value is overestimated by a factor of 3.7. For $n_H = 10^5$ cm^{-3} , the analytic approach gives a good approximation of the CRIR for the majority of the parameter space if $t > 10^4$ yr. The maximum deviation between the analytic approach and the input value ($\tilde{\zeta}_2/\zeta_2 = 2.6$) appears at $t \approx 10^4$ yr and $\zeta_2 \approx 5 \times 10^{-15}$ s^{-1} . At $n_H = 10^6$ cm^{-3} , the analytic approach gives a good estimate for all the parameter space we modeled. The results suggest that the analytic approach can be used for conditions of warm dense gas, namely in HMPOs and HMCs.

4. Discussion

4.1. Robustness of the analytic approach

In the above simulations, we ignore the variation of initial element abundances (e.g., in different metallicity environments), the size of the source, and the gas density and temperature during the evolution processes. In the following sections, we discuss the robustness of the analytic approach under different cases.

4.1.1. Variation of metallicity

The variation of metallicity would change the initial abundances of heavy elements (heavier than He). We test three metallicities ($Z = 0.1, 0.3$, and $2 Z_\odot$, which correspond to low-metallicity, outer Galaxy/Large Magellanic Cloud (LMC), and the Galactic Center) with UCLCHEM at $n_H = 10^6$ cm^{-3} . The results are shown in Fig. 6. The analytic approach gives a good estimation of ζ_2 at $Z = 0.3$ and $2 Z_\odot$. However, the analytic approach starts to underestimate the value of ζ_2 at $Z = 0.1 Z_\odot$ when the CRIR is high ($\zeta_2 \geq 3 \times 10^{-15}$ s^{-1}). At $Z = 0.1 Z_\odot$, the abundances of heavy elements are reduced by a factor of 10, while the abundances of D and He remain the same. Furthermore, due to the high CRIR, key species like CO would be easily destroyed, leading to comparable or lower abundances than that of HD. Thus, the main destruction channels of H_3^+ we considered in Sect. 2 would change. The results suggest that our analytic approach may only give a lower limit for metal-poor starburst galaxies where the CRIR is supposed to be extremely high.

4.1.2. Variation of source size

In our simulations, we set the cloud radius to be 1 pc. In reality, the size of the source could change significantly in different environments. Figure 2 shows the deviation maps from 3D-PDR

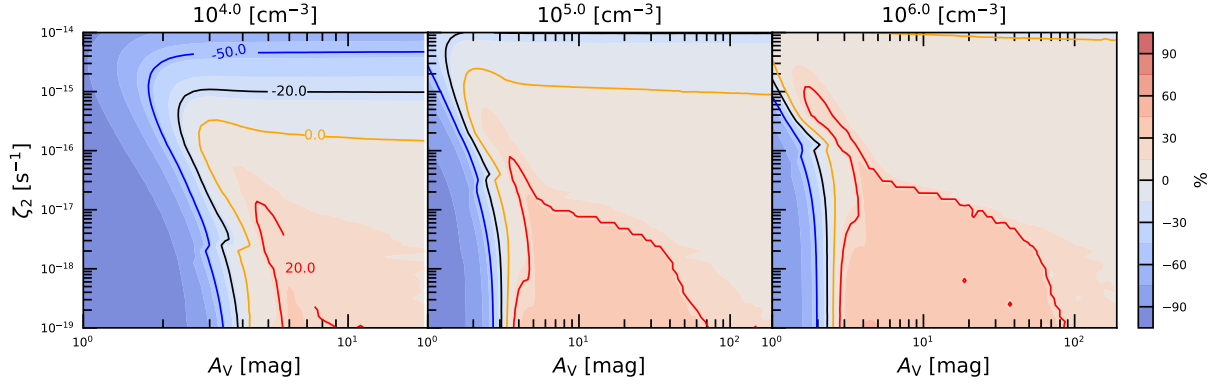


Fig. 2. Deviation maps between the analytic approaches and the input values at different A_V and ζ_2 for $n_H = 10^4$ (left), 10^5 (middle), and 10^6 cm^{-3} (right). Red, orange, black, and blue curves denote the 20, 0, -20, and -50% deviations.

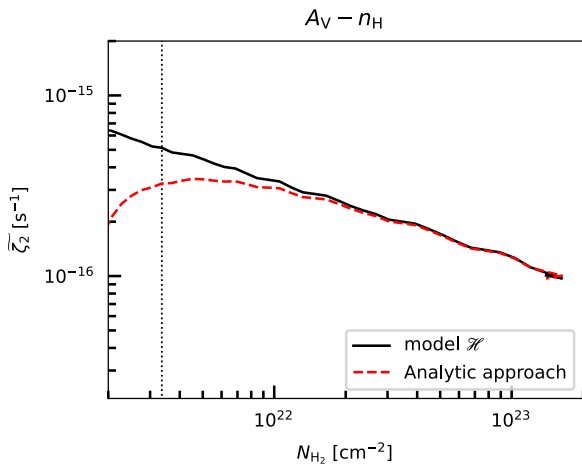


Fig. 3. Comparison of the calculated CRIR from the analytic approach (ζ_2 , red dashed curve) and the CR attenuation model (black solid curve). The vertical dashed line represents the 50% deviation between the analytic approach and the CR attenuation model.

simulations, where the analytic approach gives a good estimation of CRIR for $A_V \gtrsim 4$ mag. This value corresponds to 0.25 pc at $n_H = 10^4 \text{ cm}^{-3}$ and 2.5×10^{-3} pc (~ 500 AU) at $n_H = 10^6 \text{ cm}^{-3}$, suggesting a minimal source size that the analytic approach can give a good CRIR estimation. We also run simulations with two different source sizes ($r = 0.1, 5$ pc) in UCLHEM. As seen in Fig. 7, changing the source size has no impact on the conclusions.

4.1.3. HMC models

To test the robustness of our analytic approach, we perform tests with more physical HMC models, which consider both the variation of density and temperature with evolution timescale. Each of the HMC models consists of two stages. In the first stage, we perform simulations of the isothermal free-fall collapse (representing a prestellar phase) with an initial temperature of 10 K. The free-fall collapse phase starts from a cloud with $n_H = 10^3 \text{ cm}^{-3}$, reaching higher densities ($n_H^{\text{final}} = 10^4, 10^5$, and 10^6 cm^{-3}) at a free-fall timescale⁶ (see Priestley et al. 2018, for a detailed description of the density profiles in collapse models).

⁶ The choice of the initial density would not influence the conclusion but could greatly reduce the time cost of each simulation.

In the second stage, we perform simulations with a gradually increasing gas temperature (representing a formed HMPO or HMC) due to the heating of a central massive star. The gas densities and initial composition of all the species in the second stage inherit from the final state of the free-fall collapse. The mass of the central star in the HMC model is set to $10 M_\odot$, and the gas temperature increases from 10 to 200 K within a few 10^5 yr (see Viti et al. 2004 and Awad et al. 2010 for more details of the treatment of temperature).

Figure 8 shows the comparison between the analytic approach and the HMC models. The analytic approach gives a reasonable estimation for all models at $\zeta_2 \geq 10^{-17} \text{ s}^{-1}$, while it underestimates ζ_2 by up to a factor of 25 at $\zeta_2 \approx 10^{-18} \text{ s}^{-1}$. As shown in Fig. A.1 this is due to an underestimation of electron abundance through Eq. (2) at very low CRIR, where the formation of ions (e.g., HCO^+ and N_2H^+) is suppressed while Eq. (2) does not consider the contribution from other ions such as C^+ , Mg^+ , etc.

4.2. Uncertainties

There are a few factors that may bring uncertainties when using the analytic approach to calculate the CRIR. The most uncertain factors are the assumption of the gas phase abundances of O and N_2 , since they are almost undetectable in dense clouds. On the other hand, when there is a lack of measurements of CO isotopologs, a CO abundance of 10^{-4} (without depletion) is frequently assumed. In this section, we discuss the uncertainties induced by these factors.

Without depletion, most of the carbon is found in CO molecules in dense molecular clouds. Thus, CO has been widely used as an indicator of H_2 in large surveys (Dame et al. 2001; Su et al. 2019). The canonical abundance of CO in well-shielded molecular clouds (e.g., $A_V > 4$ mag) is $\approx 10^{-4}$ (Frerking et al. 1982; Pineda et al. 2010; Luo et al. 2023a). The calculated abundances of CO toward specific sightlines could also be biased by the method of deriving the column densities, excitation, and optical depths.

The abundance of molecular oxygen (O_2) from both observations and chemical models is negligible compared with atomic oxygen in dense clouds (Larsson et al. 2007; Goldsmith et al. 2011; Wakelam et al. 2019). Thus, the majority of the oxygen element should be in the atomic form in dense clouds. The measured mean value of atomic oxygen abundance (with respect to total H) in the moderate density cloud ($n_{\text{H}_2} = \text{a few } 10^4 \text{ cm}^{-3}$) is $(2.51 \pm 0.69) \times 10^{-4}$ (Lis et al. 2023).

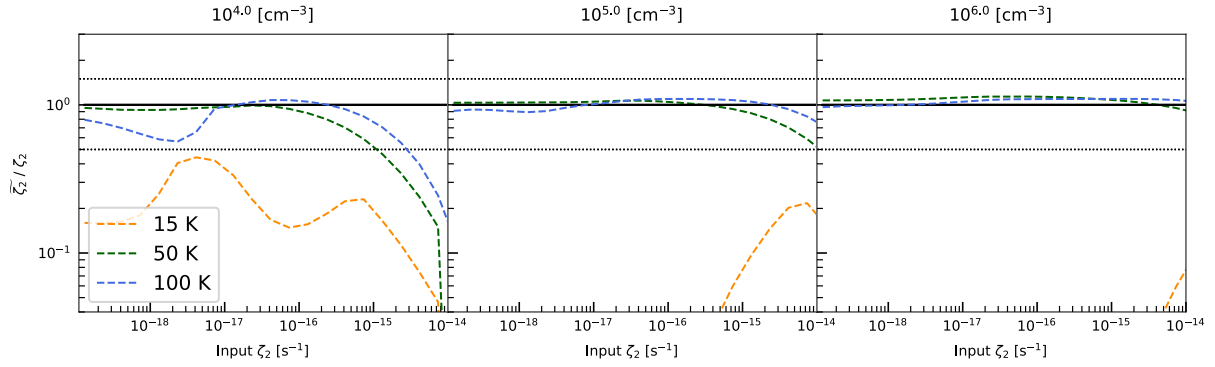


Fig. 4. Comparison between our approach and the UCLCHEM simulations. The x -axis denotes the input CRIR of each simulation, where the CRIR in each simulation is treated as uniform. The y -axis denotes the ratio between the calculated CRIR and the input one ($\tilde{\zeta}_2/\zeta_2$) at $t = 10^6$ yr. The black horizontal line represents the fiducial value and the horizontal dotted lines represent 50% of the deviation from the input values. Orange, green, and blue dashed lines represent results at $T_k = 15, 50$, and 100 K. Columns from left to right represent simulations with the cloud densities $n_H = 10^4, 10^5$, and 10^6 cm^{-3} . The large deviation at 15 K is due to the freeze-out processes that greatly reduce the gas-phase abundances of key species such as CO, thus, the chemical reactions we described in Sect. 2 are no longer satisfied.

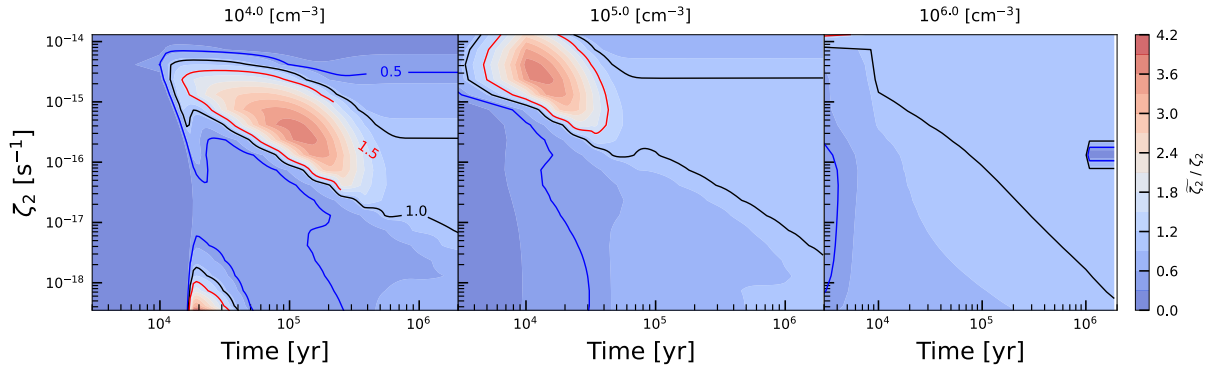


Fig. 5. Deviation maps between the analytic approaches and the input values at different evolution timescales and ζ_2 for $n_H = 10^4$ (left), 10^5 (middle), and 10^6 cm^{-3} (right). Red, black, and blue curves denote the 50, 0, and -50% deviations.

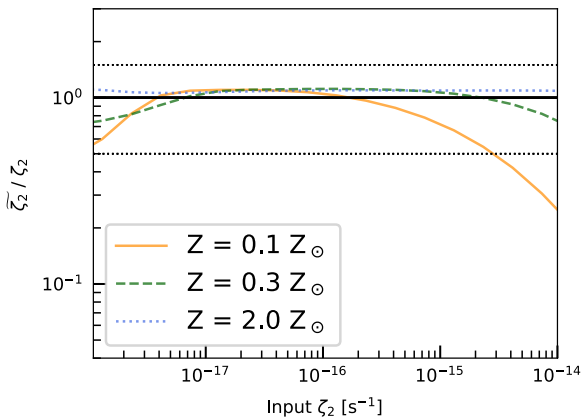


Fig. 6. Comparison between our approach and UCLCHEM simulations under different metallicities (Z). The temperature and density are adopted as 100 K and 10^6 cm^{-3} . The solid, dash, and dotted lines represent $Z = 0.1, 0.3$, and $2.0 Z_\odot$. The black horizontal line represents the fiducial value and the horizontal dotted lines represent 50% of the deviation from the input values.

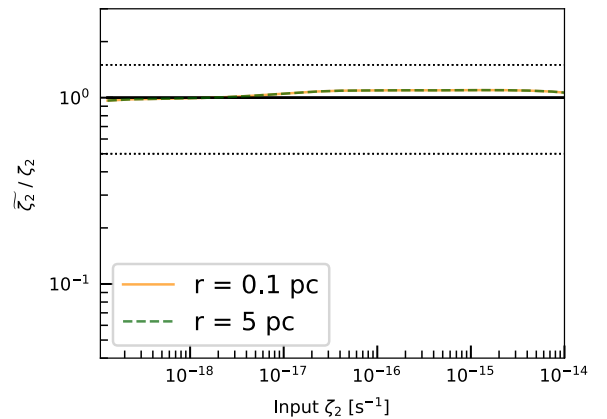


Fig. 7. Comparison between our approach and UCLCHEM simulations under different source size ($r = 0.1$ and 5 pc). The temperature and density are adopted as 100 K and 10^6 cm^{-3} . The solid and dash lines represent $r = 0.1$ and 5 pc, respectively. The black horizontal line represents the fiducial value and the horizontal dotted lines represent 50% of the deviation from the input values.

Since there are no observable rotational or vibrational transitions of N_2 in dense clouds, the main reservoir of nitrogen in molecular clouds is still under debate (Womack et al. 1992; Maret et al. 2006; Furuya & Persson 2018). Measurements from

N_2H^+ in different environments suggest that N_2 should be abundant in dense regions (Womack et al. 1992; Furuya & Persson 2018).

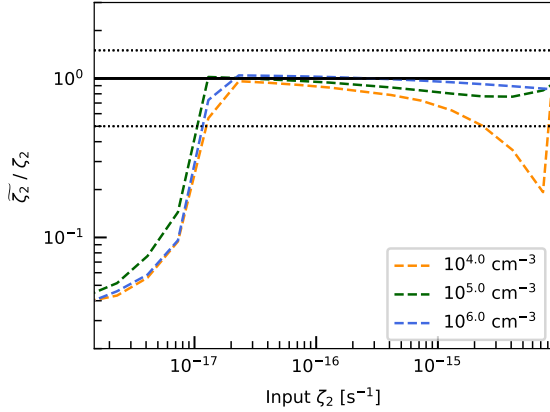


Fig. 8. Comparison of $\tilde{\zeta}_2/\zeta_2$ as a function of the input ζ_2 in the HMC models. Orange, green, and blue lines represent results at $n_{\text{H}} = 10^4, 10^5, 10^6 \text{ cm}^{-3}$. Dashed horizontal lines represent the 50% deviation from the input values.

To examine the uncertainties of CRIR induced by CO and O abundances, and whether the assumed abundances of N_2 are reasonable, we calculate the CRIR for each of the above chemical simulations, with the abundances (with respect to total H, including the uncertainties) of CO, O, and N_2 to be $(1.0 \pm 0.3) \times 10^{-4}$, $(2.51 \pm 0.69) \times 10^{-4}$, and $(3.8 \pm 0.5) \times 10^{-5}$. Figure 9 shows the mean value (dashed lines) and 1σ deviation (shadow regions) of our analytic approach with comparison to the input ζ_2 from 3D-PDR, isothermal simulations from UCLCHEM, and HMC simulations from UCLCHEM, respectively. As can be seen, the derived mean values of CRIR are mostly within 50% deviation for 3D-PDR and HMC simulations with UCLCHEM even if we consider the uncertainties induced by CO, O, and N, and the results in Sect. 3 remain the same.

Larger differences can be found in isothermal simulations with UCLCHEM. For high-temperature models ($T_{\text{k}} = 50, 100 \text{ K}$) with ζ_2 between 10^{-17} to 10^{-14} s^{-1} , the mean value is consistent with that of Fig. 4 and the deviation induced by the above uncertainties are mostly within 50%. When ζ_2 below a few 10^{-18} s^{-1} , the deviation induced by the above uncertainties would tend to decrease the calculated CRIR by up to a factor of ~ 10 . The results suggest that the assumed initial abundances of O or N_2 deviate from the simulations at low CRIR. For low-temperature models ($T_{\text{k}} = 15 \text{ K}$), the predicted mean value is significantly different from the previous results in Fig. 4, suggesting an unpredictable behavior at the low temperature and the analytic approach should not be used in such environments. In the following analysis, we consider all the above uncertainties when calculating the CRIR using Eq. (11).

4.3. Comparison between our calculations and the literature

We apply our method to two well-known sources (OMC-2 FIR 4 and L1157-B1) with reported CRIR values found in the literature. The two sources have available HCO^+ and N_2H^+ observations, and the source physical properties are located within the allowable parameter space as we discussed above.

4.3.1. OMC-2 FIR 4

At a distance of $\sim 420 \text{ pc}$ (Hirota et al. 2007), OMC-2 FIR 4 is located in the north of the Orion KL object, which hosts a few embedded low- and intermediate-mass protostars (Shimajiri et al. 2008). Multi-transitions of N_2H^+ ($J=6-5$ to $12-11$), HCO^+

($J=6-5$ to $13-12$), and H^{13}CO^+ ($J=6-5$ to $7-6$) have been observed toward this source with *Herschel*. The detailed spectral line energy distribution (SLED) analysis can be found in Ceccarelli et al. (2014b).

The non-local thermal equilibrium (LTE) results for the warm core component and the envelope are taken from Table 1 in Ceccarelli et al. (2014b). The column density of H_2 (N_{H_2}) has relatively larger uncertainties than those of molecular lines. The value of N_{H_2} derived from the modeled source size ($\sim 1600 \text{ AU}$) in Ceccarelli et al. (2014b) is $9.6 \times 10^{23} \text{ cm}^{-2}$. However, this value is higher than that given by radiative transfer modeling of dust spectral energy distribution (SED, $N_{\text{H}_2} = 2.2 \times 10^{23} \text{ cm}^{-2}$, Crimier et al. 2009) and that measured from 3 mm continuum ($1-9 \times 10^{23} \text{ cm}^{-2}$, Fontani et al. 2017). In regards to the 3 mm continuum, which could be contributed by both free-free emission and dust thermal emission, the derived N_{H_2} should be considered as an upper limit.

On the other hand, due to the lack of velocity information in the dust continuum, the core and envelope components cannot be distinguished. To simplify our calculations, a median value of $N_{\text{H}_2} = (5 \pm 1.3) \times 10^{23} \text{ cm}^{-2}$ is adopted for the warm core component (which is the dominant component). The minimum and maximum values of N_{H_2} adopted are $1 \times 10^{23} \text{ cm}^{-2}$ and $9 \times 10^{23} \text{ cm}^{-2}$, respectively. For the envelope component, the value of $N_{\text{H}_2} = 6.6 \times 10^{22} \text{ cm}^{-2}$ is adopted according to the models presented in Ceccarelli et al. (2014b).

Following Eq. (11), the derived CRIR toward the warm core component is $\zeta_2 = (1.0 \pm 0.3) \times 10^{-14} \text{ s}^{-1}$, with a lower limit of $(0.6 \pm 0.2) \times 10^{-14} \text{ s}^{-1}$ (adopting $N_{\text{H}_2} = 9 \times 10^{23} \text{ cm}^{-2}$) and an upper limit of $(5.2 \pm 1.4) \times 10^{-14} \text{ s}^{-1}$ (adopting $N_{\text{H}_2} = 1 \times 10^{23} \text{ cm}^{-2}$). The models of Ceccarelli et al. (2014b) result in a CRIR more than two orders of magnitude higher than ours (they find $\zeta_2 \sim 6 \times 10^{-12} \text{ s}^{-1}$). We argue that this may be related to their overestimation of N_2H^+ and HCO^+ abundances by 2–3 orders of magnitude. According to the non-LTE analysis in Ceccarelli et al. (2014b), the calculated abundances of HCO^+ and N_2H^+ should be 7.3×10^{-11} and 3.1×10^{-11} , respectively. However, the resultant abundances of HCO^+ and N_2H^+ from their chemistry analysis are 10^{-7} and 3×10^{-8} . The derived CRIR toward the envelope is $\zeta_2 = (1.0 \pm 0.3) \times 10^{-14} \text{ s}^{-1}$, which is slightly lower than the value given by Ceccarelli et al. (2014b, $\zeta_2 = 1.5-8 \times 10^{-14} \text{ s}^{-1}$) and recent chemical modeling from carbon-chain molecules ($\zeta_2 \approx 4 \times 10^{-14} \text{ s}^{-1}$, Fontani et al. 2017; Favre et al. 2018).

4.3.2. L1157-B1

L1157-B1 is a well-known line-rich shock region, which is located at the blue-shifted outflow lobe of a low-mass protostar L1157 (Bachiller & Pérez Gutiérrez 1997; Lefloch et al. 2017; Holdship et al. 2019; Codella et al. 2020). Various molecular line emissions (e.g., CH_3OH , SiO) have been detected toward L1157-B1 with broad linewidth (a few to $\sim 20 \text{ km s}^{-1}$) and enhanced abundance respect to H_2 . High sensitivity IRAM 30-m observations found broad linewidth ($4.3 \pm 0.2 \text{ km s}^{-1}$) emission of N_2H^+ , while the calculated abundance of N_2H^+ has large uncertainties due to the unknown kinetic temperature (Codella et al. 2013; Podio et al. 2014).

Recent NH_3 observations by JVLA had revealed the distribution of T_{k} at the blue-shifted lobe of L1157 (Feng et al. 2022). In the B1 regions, T_{k} is in the range of $80-120 \text{ K}$. We take an average T_{k} to be 100 K within the $26''$ IRAM beam-size toward L1157-B1, and a consistent n_{H_2} of 10^5 cm^{-3} as in Podio et al. (2014). We use the non-local thermal equilibrium (LTE) radiative transfer model RADEX (van der Tak et al. 2007)

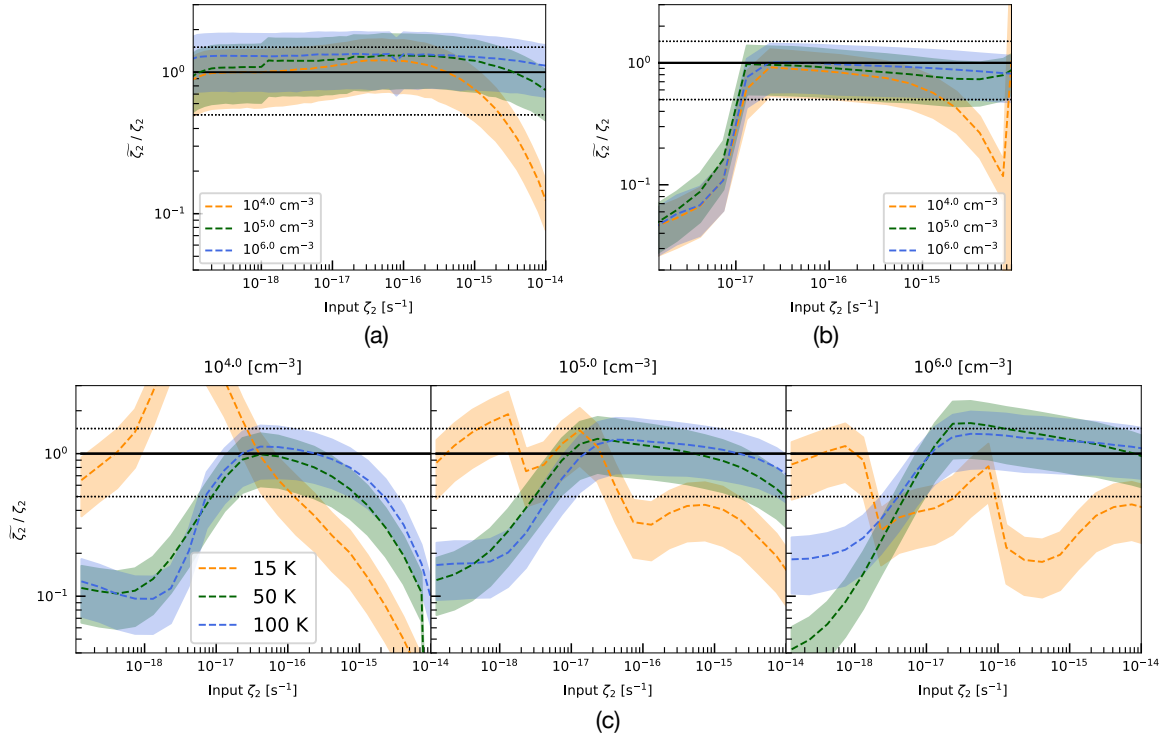


Fig. 9. Comparison of $\tilde{\zeta}_2/\zeta_2$ and uncertainties induced by gas phase abundances of CO, O, and N₂ for (a) 3D-PDR simulations, (b) HMC simulations from UCLCHEM, and (c) isothermal cloud simulations from UCLCHEM. The dashed curves and the shadow regions represent the mean value and 1σ deviation from our calculation. Orange, green, and blue lines represent different densities (in (a) and (b)) or temperatures (in (c)). Dashed horizontal lines represent 50% deviation from the input ζ_2 .

to calculate the column density. The collisional excitation rate coefficients of N₂H⁺ from Daniel et al. (2005) are adopted and obtained from the Leiden Atomic and Molecular Database (LAMDA, Schöier et al. 2005). The derived column density of N₂H⁺ is $(9.2 \pm 1.0) \times 10^{11} \text{ cm}^{-2}$, and the resultant abundance is $(9.2 \pm 1.0) \times 10^{-10}$. The abundances of CO and HCO⁺ are 1×10^{-4} and 7×10^{-9} , respectively (Podio et al. 2014). The derived CRIR toward L1157-B1 from Eq. (11) is $\zeta_2 = (2.2 \pm 0.4) \times 10^{-16} \text{ s}^{-1}$, which is in good agreement with the value from chemical modeling ($\zeta_2 \approx 3 \times 10^{-16} \text{ s}^{-1}$, Podio et al. 2014; Benedettini et al. 2021).

5. The CRIR in HMSFRs

To statistically investigate how the CRIR varies in different stages of HMSFRs, we calculate CRIR using our method toward a total of 82 samples from Purcell et al. (2006, 2009) and Gerner et al. (2014, 2015). These samples include 20 HMPOs, 54 HMCs, and 8 ultra-compact H II (UCH II) regions.

In the hot core samples of Purcell et al. (2006, 2009), the gas temperatures are in the range of 28 ± 7 to 131 ± 53 K, which are derived from the rotational diagram of CH₃CN. The column densities of HCO⁺ are derived from the optically thin H¹³CO⁺ emission, assuming $^{12}\text{C}/^{13}\text{C} = 50$ and $T_{\text{ex}} = 50$ K. The column densities of N₂H⁺ are derived from the hyperfine transitions with the assumption of $T_{\text{ex}} = 10$ K and are corrected for the beam dilution with dust continuum. The column and volume densities of H₂ are derived from 1.2 mm continuum emission (see Purcell et al. (2009) for details). There are no observations of CO isotopologs, in our calculation, a constant abundance of CO ($1.0 \pm 0.3 \times 10^{-4}$) is assumed for all the hot core samples from Purcell et al. (2006, 2009).

In the samples of Gerner et al. (2014, 2015), the gas temperatures of HMPOs, HMCs, and UCH II are 29.5, 40.2, and 36 K, respectively. The column densities of HCO⁺ are derived from two transitions of H¹³CO⁺ (1–0 and 3–2) using RADEX, assuming $^{12}\text{C}/^{13}\text{C} = 89^7$. The column densities of N₂H⁺ are calculated with the hyperfine structure fitting routine. The column densities of CO are derived from C¹⁸O with LTE, assuming $^{16}\text{O}/^{18}\text{O} = 500$. The H₂ column densities are derived from dust emission at 850 μm with JCMT or 1.2 mm with IRAM-30 m (see Gerner et al. (2014) for details). The volume densities of H₂ are derived by assuming a typical source size of 0.5 pc for all sources. We note that the choice of source size is based on the IRAM-30 m beam size, which may underestimate the actual physical size of these systems. Thus, the derived CRIR may also be underestimated.

Figure 10 shows the calculated ζ_2 from the above samples. For comparison, the CRIR values from L1544 (Redaelli et al. 2021) and IRDC G28.37+00.07 (Entekhabi et al. 2022), and the theoretical CR attenuation models \mathcal{L} , \mathcal{H} , and \mathcal{U} from Padovani et al. (2024) are also overlaid. The models \mathcal{L} , \mathcal{H} , and \mathcal{U} are based on different assumptions on the low-energy slope of the interstellar CR proton spectrum (see Ivlev et al. 2015 and Padovani et al. 2024 for a detailed description of the parameterization of the CR spectrum), which have energy density $\varepsilon_{\text{CR}} \approx 0.65, 1.18, \text{ and } 2.28 \text{ eV cm}^{-3}$, respectively. The trends of the CRIR in Fig. 10 also account for the ionization due to primary and secondary electrons. It is noted that all the physical parameters ($T_{\text{kin}} \geq 30$ K, $n_{\text{H}_2} > 10^4 \text{ cm}^{-3}$, no CO depletion) are within

⁷ Although the adopted value is higher than the local interstellar medium (ISM) (~ 65 , Milam et al. 2005) and those from Purcell et al. (2006, 2009), a variance of $^{12}\text{C}/^{13}\text{C}$ by 30% would only result in an uncertainty of ζ_2 by $\sim 1\%$.

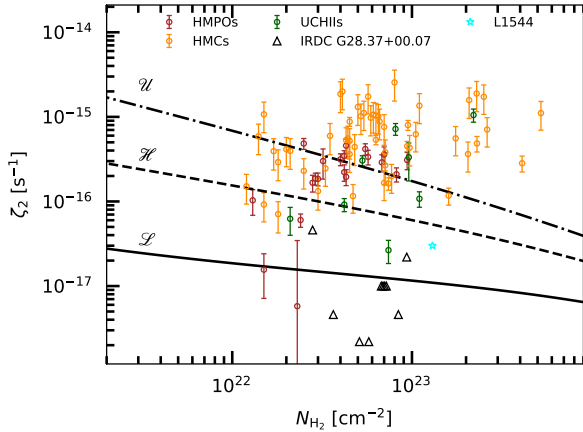


Fig. 10. Calculated ζ_2 toward HMPOs (brown), HMCs (orange), and UCH IIs (green). Black triangles represent CRIR from IRDC G28.37+00.07, which are taken from Entekhabi et al. (2022). The cyan star represents CRIR from prestellar core L1544, which is taken from Redaelli et al. (2021). The black solid, dashed, and dash-dotted curves denote the theoretical CR attenuation models \mathcal{L} , \mathcal{H} , and \mathcal{U} by Padovani et al. (2024).

the allowable parameter space that the analytic approach gives a good approximation. The average values of ζ_2 in HMPOs, HMCs, and UCH II are $(2.5 \pm 1.3) \times 10^{-16}$, $(7.4 \pm 5.0) \times 10^{-16}$, and $(3.4 \pm 3.4) \times 10^{-16} \text{ s}^{-1}$, respectively. The values in these targets are over an order of magnitude higher than the measurements in prestellar cores (e.g., L1544 and G28.37+00.07) and that predicted by the model \mathcal{H} , where the latter describes the average decrease of the observationally estimated ζ_2 (Padovani et al. 2022; Padovani 2023).

Interestingly, observations from *Fermi* and the Large High Altitude Air Shower Observatory (LHAASO) also find the ubiquitous γ -ray emissions in HMSFRs (e.g., W43) from sub-GeV to PeV (Yang et al. 2018; Yang & Wang 2020; Vink 2022; de la Fuente et al. 2023), suggesting an efficient acceleration of particles in active star-forming environments (Bykov et al. 2020; Tibaldo et al. 2021; Owen et al. 2023). While the high energy ($E \gg 10 \text{ GeV}$) γ -ray could originate from CRs accelerated by stellar wind of massive stars (Peron et al. 2024), the lower energy γ -ray could come from the embedded massive protostars which undergo their accretion phase and in which the first-order Fermi acceleration mechanism operates, e.g., jet shocks (Padovani et al. 2015, 2016; Lattanzi et al. 2023), shocks on protostellar surfaces (Padovani et al. 2015, 2016; Gaches & Offner 2018), H II regions (Padovani et al. 2019; Meng et al. 2019), and wind-driven shocks (Bhadra et al. 2022). These processes would accelerate CRs to tens of GeV (depending on the actual physical conditions), leading to a detectable γ -ray emission toward individual protostar (Araudo et al. 2007; Bosch-Ramon et al. 2010; Padovani et al. 2015, 2016). The detection of γ -ray emission at $\sim 1 \text{ GeV}$ from the protostellar jet in HH 80-81 and $\sim 10 \text{ GeV}$ level toward a young massive protostar supports these scenarios (Yan et al. 2022; de Oña Wilhelmi et al. 2023).

The high values of ζ_2 from our work are also consistent with the model prediction under the existence of internal CR source models as presented by Gaches et al. (2019), in which the CRIR is in the range of 10^{-16} s^{-1} – 10^{-14} s^{-1} at a column density of $\sim 10^{23} \text{ cm}^{-2}$. In addition, observations toward B335 also suggest high CRIR near the central protostars (Cabedo et al. 2023). The increasing trend of CRIR from HMPOs to HMCs is consistent with our understanding that HMCs are in a more evolved phase

and that star-formation activities (e.g., shocks) in HMCs may have stronger impacts on the surrounding gas. At the late stage of HMSFRs, once the central massive protostars have gathered enough mass and evolved to the zero age main sequence, the stellar wind and radiation feedback would drive the surrounding gas and lead to an expansion of UCH II regions. And because the accretion and outflows/jets gradually disappear in the late stage, the CRIR could be lower.

Such a methodology could be, in principle, used to estimate CRIR of external galaxies, where the physical properties could be quite different to those in the Milky Way (Rosolowsky et al. 2021). However, we should note that a better understanding of the source properties (e.g., density, metallicity) and a correction for the beam dilution are needed before using such a method on distant starburst galaxies. This is because, the spatial resolution of distant galaxies is usually quite low, thus, the average volume density within the beam is not supposed to be high enough to give a good approximation at very high CRIR ($\zeta_2 \geq 10^{-14} \text{ s}^{-1}$, see Sect. 3). For cosmic noon starburst galaxies where the CRIR is supposed to be extremely high (e.g., orders of magnitude above $\sim 10^{-16}$ – 10^{-14} s^{-1} , Indriolo et al. 2018), the analytic approach could only give a lower limit.

6. Conclusions

We present a new analytic approach to estimate the CRIR using the abundances of HCO^+ , N_2H^+ , and CO. The basic assumptions of deriving the analytic approach are: 1) HCO^+ , N_2H^+ , H_3^+ , and H_3O^+ are the main ions, and 2) warm gas environments (depletion of molecules can be ignored). Our analytic approach has been tested with different 3D-PDR and UCLCHEM simulations. The main conclusions are as follows:

1. The analytic approach gives a reasonable estimation of ζ_2 (to within 50% deviation) in dense warm gas (e.g., $n_{\text{H}} \geq 10^4 \text{ cm}^{-3}$, $T \geq 50 \text{ K}$) for $A_{\text{V}} \geq 4 \text{ mag}$, $t \geq 2 \times 10^4 \text{ yr}$. The higher the gas density, the better the estimation from our analytic approach. Such environments may correspond to HMPOs and HMCs.
2. Application of our method to the OMC-2 FIR 4 envelope and L1157-B1 results in ζ_2 values of $(1.0 \pm 0.3) \times 10^{-14} \text{ s}^{-1}$ and $(2.2 \pm 0.4) \times 10^{-16} \text{ s}^{-1}$, which are in good agreement with the estimation of ζ_2 from the chemical modeling in the literature, suggesting wide applicability of our method in warm gas environments.
3. The values of ζ_2 toward a total of 82 samples of HMPOs, HMCs, and UCH II have been derived with our analytic approach. The average value of ζ_2 in HMCs is over an order of magnitude higher than the prediction of canonical CR attenuation models. Our results suggest that the internal massive protostars are likely to be responsible for the high CRIR.

We highlight future high spatial resolution interferometry observations with multi-transitions of molecular lines, which will allow the more robust estimation and direct mapping of CRIR in HMSFRs. This will potentially help understand the origin of the high CRIR (Padovani et al. 2019, 2021).

Acknowledgements. B.A.L.G. acknowledges support from a Chalmers Cosmic Origins postdoctoral fellowship.

References

- Araudo, A. T., Romero, G. E., Bosch-Ramon, V., & Paredes, J. M. 2007, *A&A*, **476**, 1289
 Awad, Z., Viti, S., Collings, M. P., & Williams, D. A. 2010, *MNRAS*, **407**, 2511

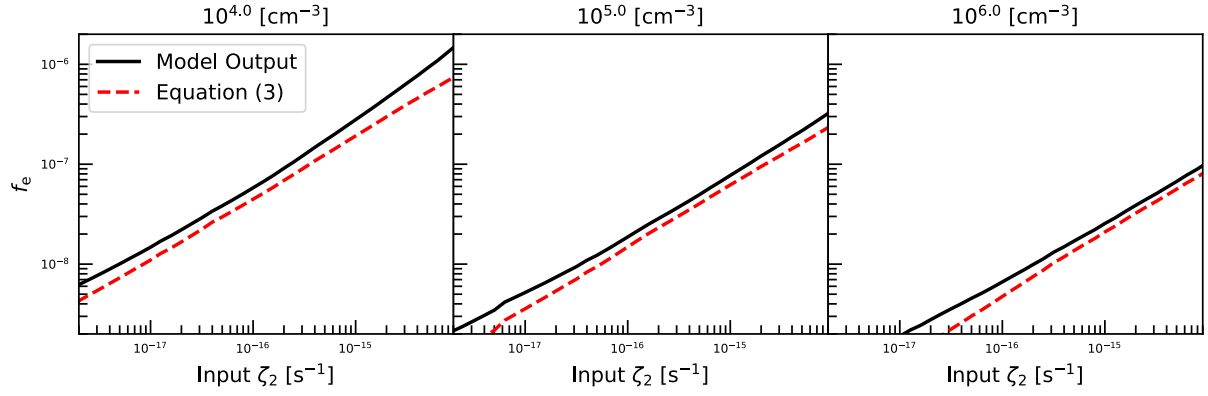
- Bachiller, R., & Pérez Gutiérrez, M. 1997, *ApJ*, **487**, L93
- Benedettini, M., Viti, S., Codella, C., et al. 2021, *A&A*, **645**, A91
- Beuther, H., Schilke, P., Menten, K. M., et al. 2002a, *ApJ*, **566**, 945
- Beuther, H., Schilke, P., Sridharan, T. K., et al. 2002b, *A&A*, **383**, 892
- Beuther, H., Churchwell, E. B., McKee, C. F., & Tan, J. C. 2007a, in *Protostars and Planets V*, eds. B. Reipurth, D. Jewitt, & K. Keil (Tucson: University of Arizona Press), 165
- Beuther, H., Zhang, Q., Bergin, E. A., et al. 2007b, *A&A*, **468**, 1045
- Bhadra, S., Gupta, S., Nath, B. B., & Sharma, P. 2022, *MNRAS*, **510**, 5579
- Bialy, S. 2020, *Commun. Phys.*, **3**, 32
- Bialy, S., & Sternberg, A. 2015, *MNRAS*, **450**, 4424
- Bialy, S., Belli, S., & Padovani, M. 2022, *A&A*, **658**, L13
- Bisbas, T. G., Bell, T. A., Viti, S., Yates, J., & Barlow, M. J. 2012, *MNRAS*, **427**, 2100
- Bisbas, T. G., Papadopoulos, P. P., & Viti, S. 2015, *ApJ*, **803**, 37
- Bisbas, T. G., van Dishoeck, E. F., Papadopoulos, P. P., et al. 2017, *ApJ*, **839**, 90
- Bisbas, T. G., van Dishoeck, E. F., Hu, C.-Y., & Schrubba, A. 2023, *MNRAS*, **519**, 729
- Blake, G. A., Sutton, E. C., Masson, C. R., & Phillips, T. G. 1987, *ApJ*, **315**, 621
- Bosch-Ramon, V., Romero, G. E., Araudo, A. T., & Paredes, J. M. 2010, *A&A*, **511**, A8
- Bovino, S., Ferrada-Chamorro, S., Lupi, A., Schleicher, D. R. G., & Caselli, P. 2020, *MNRAS*, **495**, L7
- Bykov, A. M., Marcowith, A., Amato, E., et al. 2020, *Space Sci. Rev.*, **216**, 42
- Cabedo, V., Maury, A., Girart, J. M., et al. 2023, *A&A*, **669**, A90
- Caselli, P., Walmsley, C. M., Terziava, R., & Herbst, E. 1998, *ApJ*, **499**, 234
- Caselli, P., Sipilä, O., & Harju, J. 2019, arXiv e-prints [arXiv:1905.08653]
- Ceccarelli, C., Caselli, P., Bockelée-Morvan, D., et al. 2014a, in *Protostars and Planets VI*, eds. H. Beuther, R. S. Klessen, C. P. Dullemond, & T. Henning (Tucson: University of Arizona Press), 859
- Ceccarelli, C., Dominik, C., López-Sepulcre, A., et al. 2014b, *ApJ*, **790**, L1
- Codella, C., Viti, S., Ceccarelli, C., et al. 2013, *ApJ*, **776**, 52
- Codella, C., Ceccarelli, C., Bianchi, E., et al. 2020, *A&A*, **635**, A17
- Comier, N., Ceccarelli, C., Lefloch, B., & Faure, A. 2009, *A&A*, **506**, 1229
- Dalgarno, A. 2006, *Proc. Natl. Acad. Sci.*, **103**, 12269
- Dame, T. M., Hartmann, D., & Thaddeus, P. 2001, *ApJ*, **547**, 792
- Daniel, F., Dubernet, M. L., Meuwly, M., Cernicharo, J., & Pagani, L. 2005, *MNRAS*, **363**, 1083
- de la Fuente, E., Toledano-Juarez, I., Kawata, K., et al. 2023, *PASJ*, **75**, 546
- de Oña Wilhelmi, E., López-Coto, R., & Su, Y. 2023, *MNRAS*, **523**, 105
- Entekhabi, N., Tan, J. C., Cosentino, G., et al. 2022, *A&A*, **662**, A39
- Favre, C., Ceccarelli, C., López-Sepulcre, A., et al. 2018, *ApJ*, **859**, 136
- Feng, S., Liu, H. B., Caselli, P., et al. 2022, *ApJ*, **933**, L35
- Fontani, F., Ceccarelli, C., Favre, C., et al. 2017, *A&A*, **605**, A57
- Frerking, M. A., Langer, W. D., & Wilson, R. W. 1982, *ApJ*, **262**, 590
- Friedman, S. D., Chayer, P., Jenkins, E. B., et al. 2023, *ApJ*, **946**, 34
- Furuya, K., & Persson, M. V. 2018, *MNRAS*, **476**, 4994
- Gaches, B. A. L., & Offner, S. S. R. 2018, *ApJ*, **861**, 87
- Gaches, B. A. L., Offner, S. S. R., & Bisbas, T. G. 2019, *ApJ*, **878**, 105
- Gaches, B. A. L., Bialy, S., Bisbas, T. G., et al. 2022a, *A&A*, **664**, A150
- Gaches, B. A. L., Bisbas, T. G., & Bialy, S. 2022b, *A&A*, **658**, A151
- Gerin, M., de Luca, M., Black, J., et al. 2010, *A&A*, **518**, L110
- Gerner, T., Beuther, H., Semenov, D., et al. 2014, *A&A*, **563**, A97
- Gerner, T., Shirley, Y. L., Beuther, H., et al. 2015, *A&A*, **579**, A80
- Glassgold, A. E., & Langer, W. D. 1973, *ApJ*, **179**, L147
- Goldsmith, P. F., Liseau, R., Bell, T. A., et al. 2011, *ApJ*, **737**, 96
- Herbst, E., & van Dishoeck, E. F. 2009, *ARA&A*, **47**, 427
- Hincelin, U., Wakelam, V., Hersant, F., et al. 2011, *A&A*, **530**, A61
- Hirota, T., Bushimata, T., Choi, Y. K., et al. 2007, *PASJ*, **59**, 897
- Holdship, J., Viti, S., Jiménez-Serra, I., Makrymallis, A., & Priestley, F. 2017, *AJ*, **154**, 38
- Holdship, J., Jimenez-Serra, I., Viti, S., et al. 2019, *ApJ*, **878**, 64
- Indriolo, N. 2023, *ApJ*, **950**, 64
- Indriolo, N., & McCall, B. J. 2012, *ApJ*, **745**, 91
- Indriolo, N., Neufeld, D. A., Gerin, M., et al. 2015, *ApJ*, **800**, 40
- Indriolo, N., Bergin, E. A., Falgarone, E., et al. 2018, *ApJ*, **865**, 127
- Ivlev, A. V., Padovani, M., Galli, D., & Caselli, P. 2015, *ApJ*, **812**, 135
- Kurtz, S., Cesaroni, R., Churchwell, E., Hofner, P., & Walmsley, C. M. 2000, in *Protostars and Planets IV*, eds. V. Mannings, A. P. Boss, & S. S. Russell (Tucson: University of Arizona Press), 299
- Larsson, B., Liseau, R., Pagani, L., et al. 2007, *A&A*, **466**, 999
- Lattanzi, V., Alves, F. O., Padovani, M., et al. 2023, *A&A*, **671**, A35
- Lefloch, B., Ceccarelli, C., Codella, C., et al. 2017, *MNRAS*, **469**, L73
- Linsky, J. L., Draine, B. T., Moos, H. W., et al. 2006, *ApJ*, **647**, 1106
- Lis, D. C., Goldsmith, P. F., Güsten, R., et al. 2023, *A&A*, **669**, L15
- Luo, G., Feng, S., Li, D., et al. 2019, *ApJ*, **885**, 82
- Luo, G., Zhang, Z.-Y., Bisbas, T. G., et al. 2023a, *ApJ*, **942**, 101
- Luo, G., Zhang, Z.-Y., Bisbas, T. G., et al. 2023b, *ApJ*, **946**, 91
- Majumdar, L., Gratier, P., Ruaud, M., et al. 2017, *MNRAS*, **466**, 4470
- Maret, S., Bergin, E. A., & Lada, C. J. 2006, *Nature*, **442**, 425
- McElroy, D., Walsh, C., Markwick, A. J., et al. 2013, *A&A*, **550**, A36
- Meng, F., Sánchez-Monge, Á., Schilke, P., et al. 2019, *A&A*, **630**, A73
- Meyer, D. M., Cardelli, J. A., & Sofia, U. J. 1997, *ApJ*, **490**, L103
- Meyer, D. M., Jura, M., & Cardelli, J. A. 1998, *ApJ*, **493**, 222
- Milam, S. N., Savage, C., Brewster, M. A., Ziurys, L. M., & Wyckoff, S. 2005, *ApJ*, **634**, 1126
- Millar, T. J., Bennett, A., & Herbst, E. 1989, *ApJ*, **340**, 906
- Millar, T. J., Walsh, C., Van de Sande, M., & Markwick, A. J. 2024, *A&A*, **682**, A109
- Motte, F., Bontemps, S., & Louvet, F. 2018, *ARA&A*, **56**, 41
- Neufeld, D. A., & Wolfire, M. G. 2017, *ApJ*, **845**, 163
- Neufeld, D. A., Wolfire, M. G., & Schilke, P. 2005, *ApJ*, **628**, 260
- Öberg, K. I., Boogert, A. C. A., Pontoppidan, K. M., et al. 2011, *ApJ*, **740**, 109
- Owen, E. R., Wu, K., Inoue, Y., Yang, H. Y. K., & Mitchell, A. M. W. 2023, *Galaxies*, **11**, 86
- Padovani, M. 2023, in *Physics and Chemistry of Star Formation: The Dynamical ISM Across Time and Spatial Scales* (Germany: Universitäts- und Stadtbibliothek Köln), 237
- Padovani, M., & Gaches, B. 2024, in *Astrochemical Modeling: Practical Aspects of Microphysics in Numerical Simulations*, eds. S. Bovino, & T. Grassi (Amsterdam: Elsevier), 189
- Padovani, M., Galli, D., Hennebelle, P., Commerçon, B., & Joos, M. 2014, *A&A*, **571**, A33
- Padovani, M., Hennebelle, P., Marcowith, A., & Ferrière, K. 2015, *A&A*, **582**, L13
- Padovani, M., Marcowith, A., Hennebelle, P., & Ferrière, K. 2016, *A&A*, **590**, A8
- Padovani, M., Marcowith, A., Sánchez-Monge, Á., Meng, F., & Schilke, P. 2019, *A&A*, **630**, A72
- Padovani, M., Ivlev, A. V., Galli, D., et al. 2020, *Space Sci. Rev.*, **216**, 29
- Padovani, M., Marcowith, A., Galli, D., Hunt, L. K., & Fontani, F. 2021, *A&A*, **649**, A149
- Padovani, M., Bialy, S., Galli, D., et al. 2022, *A&A*, **658**, A189
- Padovani, M., Galli, D., Scarlett, L. H., et al. 2024, *A&A*, **682**, A131
- Peron, G., Casanova, S., Gabici, S., Baghmanyan, V., & Aharonian, F. 2024, *Nat. Astron.*, **8**, 530
- Pineda, J. L., Goldsmith, P. F., Chapman, N., et al. 2010, *ApJ*, **721**, 686
- Podio, L., Lefloch, B., Ceccarelli, C., Codella, C., & Bachiller, R. 2014, *A&A*, **565**, A64
- Priestley, F. D., Viti, S., & Williams, D. A. 2018, *AJ*, **156**, 51
- Purcell, C. R., Balasubramanyam, R., Burton, M. G., et al. 2006, *MNRAS*, **367**, 553
- Purcell, C. R., Longmore, S. N., Burton, M. G., et al. 2009, *MNRAS*, **394**, 323
- Qin, S.-L., Liu, T., Liu, X., et al. 2022, *MNRAS*, **511**, 3463
- Redaelli, E., Sipilä, O., Padovani, M., et al. 2021, *A&A*, **656**, A109
- Redaelli, E., Bovino, S., Lupi, A., et al. 2024, *A&A*, **685**, A67
- Rosolowsky, E., Hughes, A., Leroy, A. K., et al. 2021, *MNRAS*, **502**, 1218
- Sabatini, G., Bovino, S., & Redaelli, E. 2023, *ApJ*, **947**, L18
- Schöier, F. L., van der Tak, F. F. S., van Dishoeck, E. F., & Black, J. H. 2005, *A&A*, **432**, 369
- Shimajiri, Y., Takakuwa, S., Saito, M., & Kawabe, R. 2008, *ApJ*, **683**, 255
- Shingledecker, C. N., Bergner, J. B., Le Gal, R., et al. 2016, *ApJ*, **830**, 151
- Sofia, U. J., Cardelli, J. A., Guerin, K. P., & Meyer, D. M. 1997, *ApJ*, **482**, L105
- Su, Y., Yang, J., Zhang, S., et al. 2019, *ApJS*, **240**, 9
- Tibaldo, L., Gaggero, D., & Martin, P. 2021, *Universe*, **7**, 141
- van der Tak, F. F. S., Black, J. H., Schöier, F. L., Jansen, D. J., & van Dishoeck, E. F. 2007, *A&A*, **468**, 627
- van Dishoeck, E. F. 2014, *Faraday Discuss.*, **168**, 9
- Vink, J. 2022, arXiv e-prints [arXiv:2212.10677]
- Viti, S., Collings, M. P., Dever, J. W., McCoustra, M. R. S., & Williams, D. A. 2004, *MNRAS*, **354**, 1141
- Wakelam, V., & Herbst, E. 2008, *ApJ*, **680**, 371
- Wakelam, V., Ruaud, M., Gratier, P., & Bonnell, I. A. 2019, *MNRAS*, **486**, 4198
- Wolfire, M. G., Hollenbach, D., & McKee, C. F. 2010, *ApJ*, **716**, 1191
- Womack, M., Ziurys, L. M., & Wyckoff, S. 1992, *ApJ*, **393**, 188
- Yan, D.-H., Zhou, J.-N., & Zhang, P.-F. 2022, *Res. Astron. Astrophys.*, **22**, 025016
- Yang, R.-Z., & Wang, Y. 2020, *A&A*, **640**, A60
- Yang, R.-Z., de Oña Wilhelmi, E., & Aharonian, F. 2018, *A&A*, **611**, A77
- Yusef-Zadeh, F., Wardle, M., Rho, J., & Sakano, M. 2003, *ApJ*, **585**, 319
- Zinnecker, H., & Yorke, H. W. 2007, *ARA&A*, **45**, 481

Appendix A: Comparison of electron fraction from our assumption and model prediction

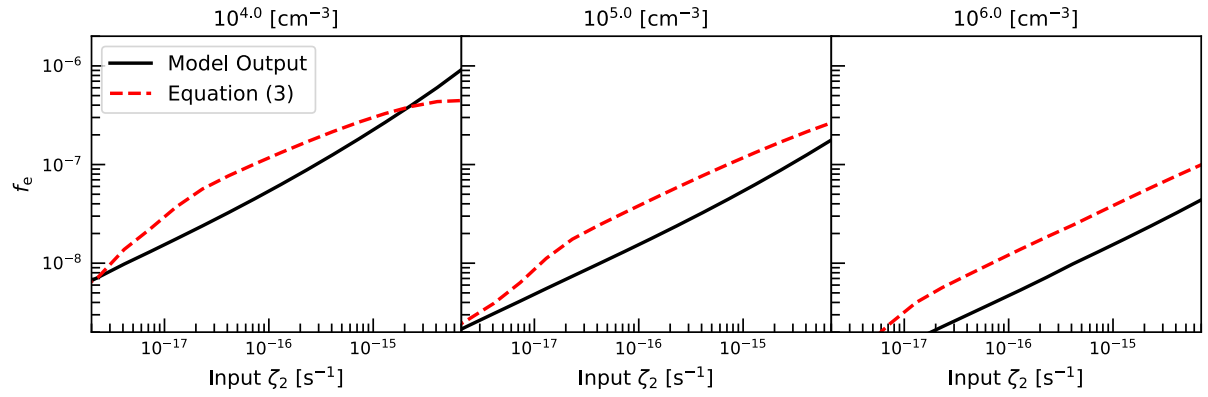
Figure A.1 shows the comparison between the electron fraction ($f(e^-)$) obtained from model simulations and that of Eq. 3. As can be seen, our assumption in Eq. 3 gives reasonable results for both 3D-PDR and UCLCHEM simulations. The deviation between Eq. 3 and model prediction is within a factor of ~ 2 for all 3D-PDR simulations and isothermal simulations from UCLCHEM. For the HMC simulations from UCLCHEM, the deviation is within a factor of 4 if $10^{-17} \leq \zeta_2/s^{-1} \leq 10^{-14}$. For $\zeta_2 < 10^{-17} s^{-1}$, Eq. 3 underestimate the electron fraction since we did not consider the contribution of other ions (e.g., C^+ , Mg^+).

Appendix B: The reaction rates that appears in the analytic approach

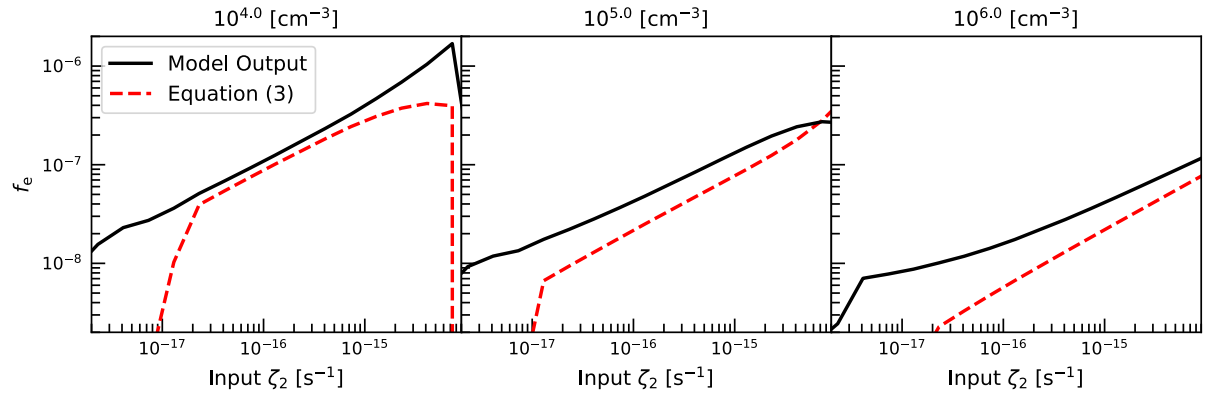
Table B.1 lists the reaction rates that appear in Sect. 2, where the rates are taken from UMIST database (Millar et al. 2024).



(a) 3D-PDR



(b) UCLCHEM (isothermal)



(c) UCLCHEM (HMC)

Fig. A.1. (a): Comparison of electron fraction as a function of ζ_2 as obtained from the 3D-PDR output (black solid curves) and from Eq. 3 (red dashed curves). (b): The same as (a) while for the isothermal simulations from UCLCHEM. (c): The same as (a) while for the HMC simulations from UCLCHEM.

Table B.1. Reaction rates of reactions in Sect. 2.

Reactions	Rates $\text{cm}^{-3} \text{ s}^{-1}$	Reactions	Rates $\text{cm}^{-3} \text{ s}^{-1}$
$\text{H}_2 + \text{CR} \longrightarrow \text{H}_2^+ + \text{e}^-$	$0.88\zeta_2$	$\text{H}_2^+ + \text{H}_2 \longrightarrow \text{H}_3^+ + \text{H}$	2.08×10^{-9}
$\text{H}_3^+ + \text{CO} \longrightarrow \text{HCO}^+ + \text{H}_2$	$1.36 \times 10^{-9} \left(\frac{T}{300}\right)^{-0.14} e^{\frac{3.4}{T}}$	$\text{H}_3^+ + \text{CO} \longrightarrow \text{HOC}^+ + \text{H}_2$	$8.49 \times 10^{-10} \left(\frac{T}{300}\right)^{0.07} e^{\frac{-5.2}{T}}$
$\text{H}_3^+ + \text{N}_2 \longrightarrow \text{N}_2\text{H}^+ + \text{H}_2$	1.8×10^{-9}	$\text{H}_3^+ + \text{O} \longrightarrow \text{OH}^+ + \text{H}_2$	$4.65 \times 10^{-10} \left(\frac{T}{300}\right)^{-0.14} e^{\frac{-0.67}{T}}$
$\text{H}_3^+ + \text{O} \longrightarrow \text{H}_2\text{O}^+ + \text{H}$	$2.08 \times 10^{-10} \left(\frac{T}{300}\right)^{-0.4} e^{\frac{-4.86}{T}}$	$\text{H}_3^+ + \text{e}^- \longrightarrow \text{H}_2 + \text{H}$	$2.34 \times 10^{-8} \left(\frac{T}{300}\right)^{-0.52}$
$\text{H}_3^+ + \text{e}^- \longrightarrow \text{H} + \text{H} + \text{H}$	$4.36 \times 10^{-8} \left(\frac{T}{300}\right)^{-0.52}$	$\text{HCO}^+ + \text{e}^- \longrightarrow \text{CO} + \text{H}$	$2.4 \times 10^{-7} \left(\frac{T}{300}\right)^{-0.69}$
$\text{N}_2\text{H}^+ + \text{CO} \longrightarrow \text{HCO}^+ + \text{N}_2$	8.8×10^{-10}	$\text{N}_2\text{H}^+ + \text{e}^- \longrightarrow \text{H} + \text{N}_2$	$3.06 \times 10^{-7} \left(\frac{T}{300}\right)^{-0.06}$
$\text{N}_2\text{H}^+ + \text{O} \longrightarrow \text{OH}^+ + \text{N}_2$	1.4×10^{-10}	$\text{OH}^+ + \text{H}_2 \longrightarrow \text{H}_2\text{O}^+ + \text{H}$	$1.27 \times 10^{-9} \left(\frac{T}{300}\right)^{0.18}$
$\text{H}_2\text{O}^+ + \text{H}_2 \longrightarrow \text{H}_3\text{O}^+ + \text{H}$	9.7×10^{-10}	$\text{H}_3\text{O}^+ + \text{e}^- \longrightarrow \text{OH} + \text{H} + \text{H}$	$3.05 \times 10^{-7} \left(\frac{T}{300}\right)^{-0.5}$
$\text{H}_3\text{O}^+ + \text{e}^- \longrightarrow \text{OH} + \text{H}_2$	$5.37 \times 10^{-8} \left(\frac{T}{300}\right)^{-0.5}$	$\text{H}_3\text{O}^+ + \text{e}^- \longrightarrow \text{H}_2\text{O} + \text{H}$	$7.09 \times 10^{-8} \left(\frac{T}{300}\right)^{-0.5}$